Fabrication of ultrafine metastable Ru-B alloy for catalytic hydrogenation of NEC at room temperature

Qijun Pei [a], Jiafeng Yu [a], Guanghao Qiu [a], Khai Chen Tan [a,b], Junfeng Wen [c], Yang Yu [a], Jintao Wang [a,b], Jiaquan Guo [a,b], Jianping Guo [a], Li Rao [d,*], Teng He [a,b,**], Ping Chen [a,b,e]

[a] Dalian Institute of Chemical Physics, Chinese Academy of Sciences, Dalian 116023, China
[b] Center of Materials Science and Optoelectronics Engineering, University of Chinese Academy of Sciences, Beijing 100049, China
[c] School of Chemistry and Chemical Engineering, Yulin University, Yulin 719000, China
[d] Hubei International Scientific and Technological Cooperation Base of Pesticide and Green Synthesis, Key Laboratory of Pesticide & Chemical Biology of Ministry of Education, College of Chemistry, Central China Normal University, Wuhan 430079, China
[e] State Key Laboratory of Catalysis, Dalian Institute of Chemical Physics, Chinese Academy of Sciences, Dalian 116023, China

ARTICLE INFO

ABSTRACT

Liquid organic hydrogen carriers (LOCHs) hold considerable potential for large-scale and long-distance energy/ hydrogen storage and transportation. However, due to the lack of efficient catalysts, harsh conditions are needed for the reversible hydrogen uptake and/or release of LOHCs. Herein, a one-pot method was developed to synthesize an ultrafine metastable Ru-B alloy, where the geometrical and electronic structure of Ru is well modulated by B. To our delight, the hydrogenation of N-ethylcarbazole (NEC, one of the promising LOHC candidates) could be catalyzed by Ru-B alloy with ca. 99 % yield to 12H-NEC at room temperature. To the best of our knowledge, this is the first example of realizing the hydrogenation of NEC at room temperature. Theoretical simulations indicate that the (0001) surface of Ru_7B_3 crystal may be the active site for the catalytic hydrogenation. This work shows the potency of metastable nanomaterials as efficient catalysts for chemical transformations which are kinetically challenging.

1. Introduction

Utilization of liquid organic hydrogen carriers (LOHCs) for large-scale and long-distance energy/hydrogen storage and transportation has been demonstrated in different countries [1,2], thanks to their low-cost, good reversibility, high hydrogen capacity, and compatibility with existing gasoline infrastructure [3–5]. One of the most promising candidates among these LOHCs is the N-ethyl-carbazole/dodecahydro-N-ethylcarbazole (NEC/12H-NEC) pair, which has a hydrogen capacity of 5.8 wt% and superb thermodynamic properties for hydrogen uptake and release [6–10]. Due to the high kinetic barriers in the reversible processes and the significant demand for efficient catalysts for both hydrogenation and dehydrogenation, tremendous research efforts have been made in this area from both fundamental research and industrial application for achieving practical applications. Until now, a number of strategies for designing catalyst have been reported for the reversible hydrogen storage of NEC/12H-NEC pair. For instance, fabrication of fully exposed palladium clusters without the presence of spectators could help maximize reactivity and atomic efficiency for the dehydrogenation of 12H-NEC [2]. Bifunctional catalysts composed of rare earth hydride and transition metal could achieve high-efficiency, reversible hydrogen storage in NEC [11–14]. The alloy catalysts (such as Ru-Pd/Al$_2$O$_3$) exhibit enhanced activity, selectivity, and stability compared with their single metal counterparts in the reversible hydrogen storage of NEC/12H-NEC pair [15–18]. The singe atom catalysts also show high-efficiency performances in the hydrogenation of NEC at a low temperature or with a low activation energy [19,20]. However, challenges still exist, i.e., harsh operational conditions (such as high temperatures and/or high hydrogen pressures) for the catalysis were usually needed, far from the requirements of practical application. For instance, the catalytic hydrogenation of NEC, which is favorable at room temperature from a thermodynamic point of view, however, usually conducted at a temperature higher than 90 °C [13, 19–21]. Therefore, room temperature

---

* Corresponding author.
** Corresponding author at: Dalian Institute of Chemical Physics, Chinese Academy of Sciences, Dalian 116023, China.
  E-mail addresses: raoli@ccnu.edu.cn (L. Rao), heteng@dicp.ac.cn (T. He).

hydrogenation of NEC is desired and long-sought, whereby the development of novel and efficient catalysts is urgently needed.

Amorphous metal-metalloid alloys have been investigated for decades in heterogeneous catalysis [22,23]. Among them, metal-boron alloys have gained much attention for their wide applications in petrochemical, fine chemical, energy, and environmental-related reactions [24–27] due to their unique properties, i.e., (1) the long-range disorder with a high concentration of low-coordination sites, namely the terrace, step, and kink sites; (2) tunable electronic structures of metal because of their diverse composition and structure; and (3) metastable nature of these amorphous alloys for their high activity in catalysis [28,29]. Consequently, it is worth adopting an amorphous boron-based alloy for the catalytic hydrogenation and dehydrogenation of LOHCs. Nevertheless, the attempts for this topic are extremely sparse. It was reported that Ru-based catalysts were often employed for the catalytic hydrogenation of NEC, although catalytic performances still have to be improved [9,16, 30]. Considering the advantages as mentioned above, alloying a Ru-based catalyst with boron could alter its geometric and electronic structures, forming a metastable alloy and leading to a significant improvement in the catalytic properties of the catalyst.

Here, a one-pot method was developed to prepare amorphous metastable Ru-B alloy nanoparticles via mechanical milling, which avoids the use of a protecting agent or support and significantly simplifies the conventional synthetic procedure. XRD, XAFS, XPS, and TEM showed that the morphology and the electronic structure of Ru was well regulated by B, leading to electronic-rich state of Ru. More importantly, this amorphous Ru-B alloy exhibited superior catalytic activities in the hydrogenation of NEC, allowing for the first time that room temperature hydrogenation of NEC to be achieved in the present study with ca. 99 % yield to 12 H-NEC, and the conversion of NEC on metastable Ru-B alloy increases by ca. 90 times compared with commercial Ru/Al_2O_3 catalyst. Theoretical simulations revealed the intrinsic active site of the Ru-B alloy for the catalytic hydrogenation of NEC. The metastable catalyst developed here highlights the unique structural and electronic properties of amorphous alloy in boosting catalytic activity for hydrogenation.

2. Experimental section

2.1. Materials and catalysts syntheses

N-ethylcarbazole (99 %, Alfa Aesar), $RuCl_3$ (Ru > 47 %, Innochem), $NaBH_4$ (98 %, Sigma-Aldrich), NaH (90 %, Sigma-Aldrich), 5 % Ru/ Al_2O_3 (Alfa Aesar) and isopropanol (99.9 %, Acmec) are commercially available. 12H-NEC was synthesized by catalytic hydrogenation of NEC. Nanosized amorphous Ru-B alloy was synthesized via a one-pot method, and its synthetic route was shown in Fig. S1. Typically, 415 mg $RuCl_3$ and 378 mg $NaBH_4$ (in a molar ratio of 1:5) were mechanically milled under argon atmosphere using a planetary ball milling (Retsch PM400) with a rate of 200 rpm for 4 h at room temperature. Then, the sample was added to 500 mL of deionized water slowly while being stirred magnetically, and it was then washed three times in deionized water. Finally, the centrifuged sample was dried under vacuum to get the ultrafine Ru-B alloy. Since Ru-B alloy is not stable after drying, LiF was used to disperse and stabilize it for characterizations. For comparison, Ru nanoparticles, denoted as Ru_{NaH} hereafter, were synthesized using the similar method, but the reducing agent $NaBH_4$ was replaced by NaH.

2.2. Catalytic performances

The suspension of Ru-B alloy in water was mixed with NEC with a desired molar ratio of Ru to NEC, followed by ultrasonication for 20 min. After that, the suspension was centrifuged and dried under vacuum at room temperature to get a solid mixture of NEC and Ru-B alloy for the hydrogenation reaction. The molar ratio of Ru to NEC is calculated from the weights of Ru precursor ($RuCl_3$) and NEC. The dried sample was loaded into a stainless steel reactor, and heated up to a desired

temperature. A certain pressure of hydrogen was charged into the reactor when the temperature is stabilized. The sample after the reaction was dissolved in ethanol for gas chromatography (GC, Agilent 7890-B, HP-5 column) analysis. The hydrogenation reactions in the presence of solvent were conducted in stainless steel autoclaves. Typically, 52 mg of Ru-B alloy, 488 mg of NEC, and 20 mL of isopropanol (*i*-PrOH) were charged into the autoclave for the hydrogenation reaction. The hydrogenated products were also analyzed by GC. For the stability test, the reaction temperature, hydrogen pressure, and reaction time were set at 60 °C, 50 bar, and 5 h, respectively. For second and third cycles, another 488 mg of NEC was added without separating 12 H-NEC from the solution.

2.3. Characterizations

All the samples for X-ray absorption fine structure (XAFS) and X-ray photoelectron spectroscopy (XPS) were mixed with LiF (75 wt%) using a mortar and pestle. XAFS measurements at Ru k-edge in transmission mode were performed at SPring-8 located in Harima Science Garden City, Hyogo Prefecture. XPS measurements were performed using an Escalab 250 Xi X-ray photoelectron spectrometer (Thermo Scientific) with nonmonochromatic Al Kα radiation (photon energy, 1486.6 eV). Prior to measurements, all of the samples were exposed to air for sample transfer. For the XPS analysis, the binding energy of F at 685.7 eV [31] was used to calibrate the spectra instead of C 1 s at 284.8 eV due to the binding energy overlapping of C 1s and Ru 3d. X-ray diffraction (XRD) measurements were performed on a PANalytical X′pert diffractometer with Cu-Kα radiation (λ = 0.154 nm) at a setting of 40 kV and 40 mA. The composition of Ru and B in the Ru-B alloy were analyzed by inductively coupled plasma-optical emission spectrometer (ICP-OES, optima 7300DV, Perkin-Elmer). High resolution transmission electron microscopy (HRTEM) images were collected on a JEOL 2000EX electronic microscope operating at 120 kV. High-angle annular dark-field scanning transmission electron microscopy (HAADF-STEM) images were collected on a JEM-2100 F instrument equipped with STEM dark-field (DF) detector operating at 200 kV.

2.4. Theoretical calculations

Cluster models of two active sites on Ru_7B_3 crystal (0001) and (10$\bar{1}$0) lattice plane were extracted from the crystal structure [32]. The Gibbs free energy (calibrated to 60 °C and 70 bar) profiles were obtained at ωB97xD/6–311 +G* *(lanl2dz for Ru)//6–31 G* (lanl2dz for Ru) level of theory [33]. The nature of stationary points was verified using frequency analysis. All calculations were performed using Gaussian 09 D.01 software package [34]. The coordinates of optimized structures could be found in the uploaded Supplementary material file "structures. zip".

3. Results and discussion

3.1. Syntheses and characterizations of the ultrafine Ru-B amorphous alloy

Traditionally, the synthetic procedure of ultrafine metal-boron alloy is complicated, where organic protecting agents or supports are usually used to ensure the well dispersion of alloy [35]. It is known that the existence of protecting agents will inevitably interfere the interaction between catalyst and reactant, scarifying its catalytic performance. Therefore, a one-pot method was developed here to fabricate ultrafine amorphous Ru-B alloy without protecting agents or supports, i.e., the reduction of $RuCl_3$ by excess $NaBH_4$ through mechanical ball milling (details in experimental section). Upon washing with deionized water in the air and drying under vacuum, black powders of Ru-B alloy nanoparticles were obtained. X-ray diffraction (XRD) pattern of the

as-prepared Ru-B alloy exhibits a broad peak centered at ca. 43° (Fig. 1a), which agrees well with the unique amorphous Ru-B alloy with short-range atomic ordering [24,36,37]. In contrast, Ru nanoparticles synthesized from the reduction of NaH (Ru$_{NaH}$ for short) demonstrate weak diffraction peaks of metallic Ru.

Transmission electron microscopy (TEM) was employed to characterize the morphology of the synthesized Ru-B alloy. As shown in Fig. 2, Ru-B nanoparticles are well dispersed with an average diameter of 5.7 ± 0.9 nm. It is worth mentioning that even if no protecting agents or supports were used in the present study, the particle size here is similar to or smaller than that from literatures [24,35,38], highlighting the effectiveness of the method developed here. Selected area electronic diffraction (SAED) on the sample displays several diffraction halos (Fig. 2c), showing the formation of an amorphous alloy which is consistent with the XRD result. The element mapping results as shown in Fig. 2d to g reveal that Ru coincides very well with B and O, evidencing the formation of Ru-B alloy. The O element may come from the absorbed O_2, H_2O or BO_3^{3-} species during sample preparation, which will be elucidated in the following sections. Inductively coupled plasma-optical emission spectrometer (ICP-OES) result shows that the molar ratio of Ru to B is close to 7:2.

X-ray absorption fine structure (XAFS) technique is a sensitive tool to characterize the local structure of amorphous material. The coordination environment of Ru atoms in Ru-B alloy are monitored at Ru K-edge,

accompanied by Ru foil and RuO_2 as references. As shown in Fig. 1b, the absorption edge in the X-ray absorption near-edge structure (XANES) spectra reveal that the Ru species are different from those of Ru foil and RuO_2 references. The shape of the white line and the structure of the post-edge region are similar to RuO_2, hinting the presence of partially reduced Ru oxides or Ru-B alloy rather than metallic Ru. From the analysis of the Fourier transformed k^3-weighted extended X-ray absorption fine structure (EXAFS) in Fig. 1c, the first shell scattering at ca. 1.5 Å without phase correction corresponds to the Ru−O path. The number of Ru−O−Ru neighbors in the second coordination shell (peak at about 3.2 Å) is significantly smaller than that of the RuO_2 reference, confirming the long-range disorder property of the catalyst. Besides, a broad peak containing both Ru−Ru scattering from metallic Ru and Ru−O−Ru from Ru oxides can be observed at a distance between 1.9 and 3.2 Å. Tetragonal RuO_2 with lattice constant a=b= 4.497 Å and c= 3.105 Å as well as Ru_7B_3 alloy are used as models for the fitting EXAFS spectra at the Ru K-edge. EXAFS spectra of the Ru-B alloy can be well-fitted as shown in Table 1 and Fig. 1d, indicating the co-existence of the Ru-B alloy and oxidized Ru. In the case of the RuO_2 part in the sample, the coordination numbers (CNs) of Ru−O in the first shell of sample are 1.6 and 3.2 at distances of 1.92 and 1.96 Å, respectively, while the CN of Ru−O−Ru is 1.6 at a distance of 3.10 Å, which are all smaller than those in the RuO_2 model, suggesting the formation of nanosized RuO_2 particles. The existence of Ru-O species may be
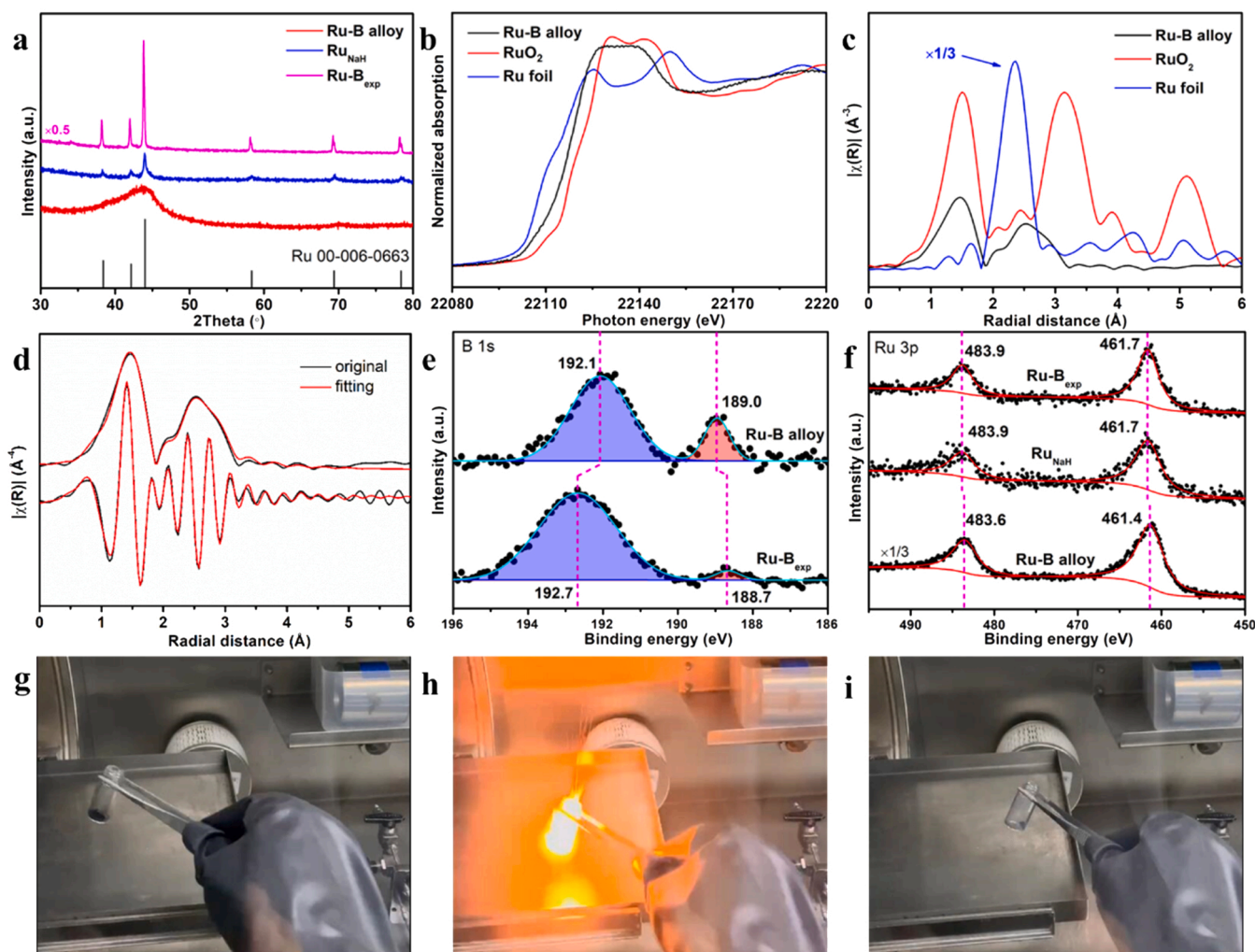

Fig. 1. (a) XRD patterns of Ru-B alloy, Ru$_{NaH}$, and Ru-B explored (Ru-B$_{exp}$ for short) samples. (b, c) Normalized XANES spectra and Fourier-transform EXAFS spectra at Ru K-edge for Ru-B alloy, RuO_2, and Ru foil. (d) XAFS fitting curve of Ru-B alloy. XPS spectra of (e) Ru 3d for Ru-B alloy, Ru$_{NaH}$, and Ru-B$_{exp}$ samples, (f) B 1 s for Ru-B alloy and Ru-B$_{exp}$ samples. Photographs of Ru-B alloy (g) before explosion, (h) in explosion and (i) after explosion.
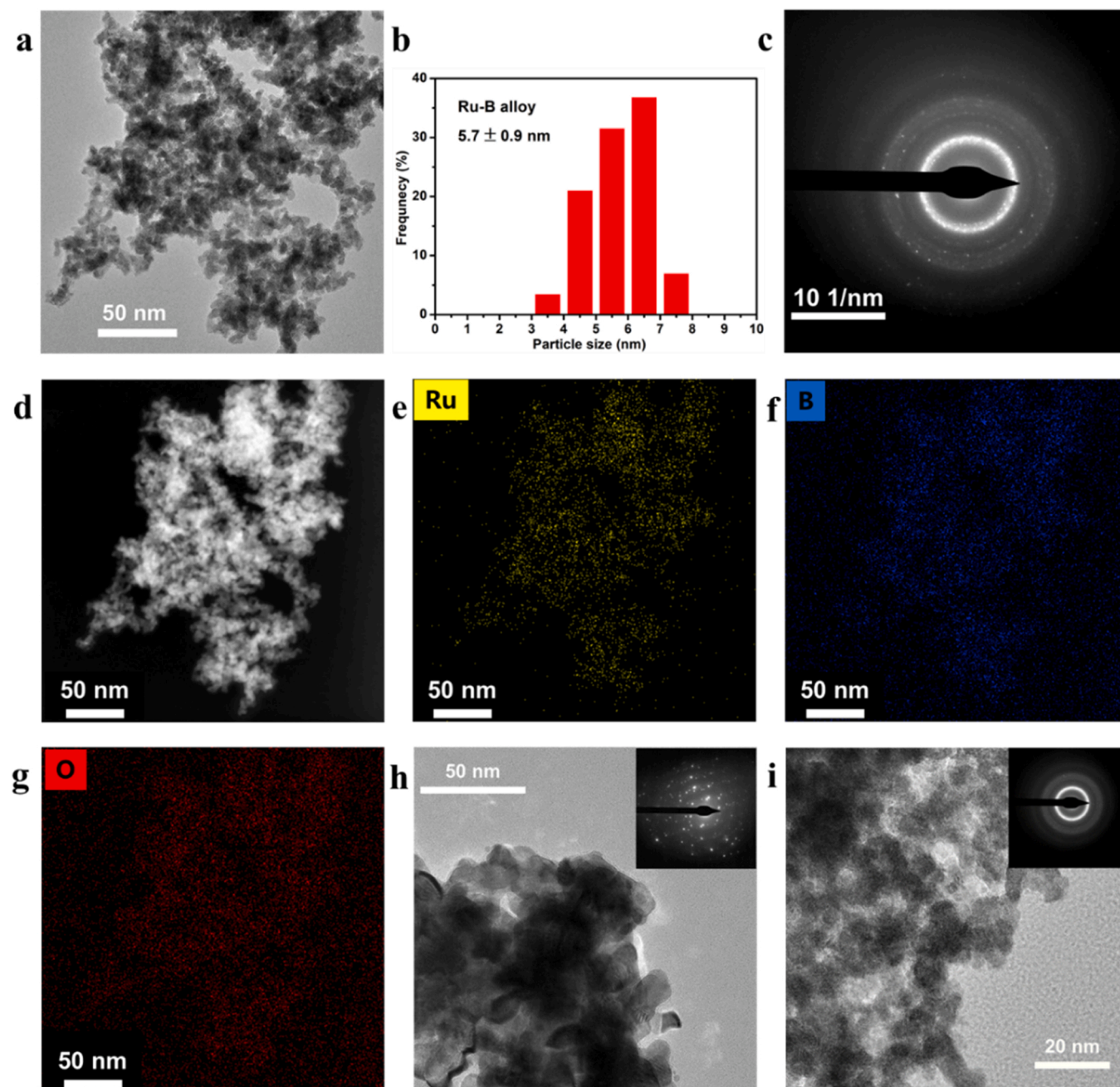
Fig. 2. (a) TEM image, (b) corresponding particle size distribution, and (c) selected-area electron diffraction pattern of Ru-B alloy. (d) HAADF-STEM image of Ru-B alloy. Ru, B, and O elemental mapping images are exhibited in (e), (f), and (g) in the HAADF-STEM image of the Ru-B alloy. TEM images of the Ru-B alloy (h) after explosion and (i) after the hydrogenation test. Inserts in panels (h) and (i) show the corresponding SAED patterns, in which the clear electron diffraction spots are observed in (h), demonstrating the formation of single crystal Ru after explosion.

Table 1

Fitting parameters resulting from analysis of Ru K-edge EXAFS for Ru-B alloy. Spectra were k^3-weighted and fitted in the range of R = 1.1–3.8 Å and k = 3.0–11.0 Å^{-1}. The amplitude reduction factor (S_0^2), as determined from Ru foil, was fixed at 0.7, and one energy shift parameter (δE_0) was defined for all scattering paths. The coordination numbers (CNs), bond lengths (R) and Debye-Waller (D.W.) factors (σ^2) were fitted as guess parameters. Standard tetragonal RuO$_2$ model with Ru-O (CN=2, R=1.942 Å; CN=4, R=1.986 Å) and Ru-Ru (CN=2, R=3.105 Å) coordination as well as Ru$_7$B$_3$ model with Ru-B (CN=3, R=2.20 Å) and Ru-Ru (CN=3, R=2.721 Å; CN=9, R=2.850 Å) coordination were used.

Samples	Ru-O/Ru-B		Ru-Ru		D. W.	ΔE_0 (eV)	R factor
	R (Å)	CN	R (Å)	CN			
Ru foil	—	—	2.65 ± 0.006 2.70 ± 0.006	6.0 ± 0.6 6.0 ± 0.6	0.0024 ± 0.0008	-3.9 ± 1.1	0.024
RuO$_2$ in sample	1.92 ± 0.02 1.96 ± 0.02	1.6 ± 0.3 3.2 ± 0.6	3.10 ± 0.01	1.6 ± 0.4	0.0040 ± 0.0012	-1.8 ± 1.4	0.023
Ru$_7$B$_3$ in sample	2.12 ± 0.02	2.9 ± 1.2	2.64 ± 0.02 2.77 ± 0.02	0.3 ± 0.1 0.9 ± 0.3	0.0040 ± 0.0012	-6.4 ± 2.8	0.023

attributed to the oxidization of Ru-B alloy through adsorption of O-species on the surface during preparation in the air. For Ru_7B_3 part in sample, the CN of Ru−B in the first shell is 2.9 at 2.12 Å, which is very close to that in the model. However, the CNs of Ru−B−Ru in the second shell are much smaller, demonstrating that the Ru_7B_3 species are highly dispersed and long-range disordered in the sample. From all above, the identification of Ru-B alloy is consistent with the results from both XRD and TEM.

The formation of Ru-B alloy is further confirmed by X-ray photoelectron spectroscopy (XPS) technique (Fig. 1e, f, and S2). The B 1 s spectrum (Fig. 1e) shows two peaks centered at 189.0 and 192.1 eV, which are attributed to B in Ru-B alloy and $[BO_3]^{3-}$ species that adsorbed on the alloy surface [24], respectively. It is notable that the binding energy of B in Ru-B alloy is ca. 0.3 eV higher than elemental B, suggesting the electron transfer from B to Ru. Due to the overlapping between C 1s and Ru 3d signals, Ru 3p spectrum is adopted to reveal the electronic structure of Ru in Ru-B alloy [39]. The binding energies of Ru $3p_{1/2}$ and $3p_{3/2}$ for Ru-B alloy are 483.6 and 461.4 eV, respectively, which are 0.3 eV lower than those of metallic Ru_{NaH}, confirming the electron donation from B to Ru [37].

All the characterizations abovementioned clearly demonstrate the successful synthesis of amorphous Ru-B nanoparticles, albeit they were partially oxidized by air. Unexpectedly, the as-prepared Ru-B alloy after being dried is highly active, which will explode upon shaking the sample (see Fig. 1g - i and Video S1). The explosive feature that has never been observed for Ru-B or other B-based alloys in literatures clearly demonstrates the fabrication of metastable alloy in the present study. The mechanical ball milling with high energy input could drive the solid reduction of Ru^{3+} by $NaBH_4$ in a short time, making B stay beside Ru and forming a kinetically stable state. The destabilizing effect of the defects created by the ball milling may result in the formation of metastable alloys [40]. For the sake of safety, the metastable Ru-B alloy was preserved in water and/or stabilized by compounds throughout all characterizations/delivery. To figure out the reason of such explosion, products after explosion (Ru-B$_{exp}$ for short) were collected and characterized. Results from XRD (Fig. 1a), TEM (Fig. 2h), and XPS (Fig. 1f) of Ru-B$_{exp}$ demonstrated clear evidences that metallic Ru was formed, showing the transformation from amorphous Ru-B alloy to crystalline Ru during explosion. Despite no B signal can be observed from XRD and TEM, the presence of a prominent peak at 192.7 eV and a very weak peak at 188.7 eV from B 1s bonding energies in XPS can be attributed to the B_2O_3 and elementary B, respectively, evidencing the oxidization of B during explosion. To confirm the function of B in the explosion, $LiBH_4$ was also employed to prepare the Ru-B alloy via the same method, and explosion was still observed after drying the alloy. However, if NaH was

used as a reducing agent, the explosion does not occur, manifesting the important role of B in the alloy. It is well known that the oxidation of B is a strong exothermic process, which can be used as explosive or propellant additives [41]. Therefore, we tentatively believe that the explosion was caused by elementary B in the metastable amorphous Ru-B alloy rapidly oxidizing to generate B_2O_3 as a result of the ultrafine particles, releasing a large amount of energy instantly. Meanwhile, amorphous and nanosized Ru species that separated by B in Ru-B alloy suddenly aggregated, which is also an exothermic process.

Supplementary material related to this article can be found online at doi:10.1016/j.apcatb.2023.122947.

3.2. Catalytic performances of the amorphous metastable Ru-B alloy

Considering the unique properties of amorphous Ru-B alloy, we evaluate its catalytic activity via the catalytic hydrogenation of NEC. For comparison, the catalytic performances of Ru_{NaH}, Ru-B$_{exp}$, and commercial Ru/Al_2O_3 were also tested. As shown in Fig. 3a, Ru-B$_{exp}$ catalyst did not result in any activity on the hydrogenation of NEC at 60 °C under 70 bar H_2. Under the same conditions, a yield of 22.3 % to 12 H-NEC was obtained when Ru_{NaH} catalyst was employed. Nonetheless, a negligible conversion was observed when the temperature decreased to 25 °C. Meanwhile, commercial Ru/Al_2O_3 also demonstrated a low activity at room temperature, i.e., a NEC conversion of 1.1% was obtained. In contrast, Ru-B alloy exhibited superior activities under the same conditions, i.e., a full conversion of NEC was achieved on Ru-B alloy catalyst at 60 °C under 70 bar H_2 in 2.5 h with a 12 H-NEC yield of 99.3% (Fig. 3a and entry 1 in Table 1). The conversion of NEC on Ru-B alloy catalyst increases by a factor of more than 15 compared with Ru nanoparticles (Ru_{NaH}) under these conditions. More excitedly, the conversions of NEC can still be reached > 99.9 % even when the temperature was decreased to 35 and 25 °C with the yields of 12 H-NEC as high as 98.1 % and 98.6 %, respectively, demonstrating ca. 90 folds enhancement as compared with that of commercial Ru/Al_2O_3 under the same condition (Fig. 3a and entries 2–3 in Table 2). It is worth noting that the hydrogenation of NEC was usually conducted in the range of 90 – 180 °C in previous literatures (Table S1) [19,21], and this is the lowest temperature at which a full conversion of NEC could be achieved in the present investigation with such a high yield of 12 H-NEC. Furthermore, when the hydrogen pressure was reduced, the Ru-B alloy could still demonstrate attractive activities (entries 4–6). Even if the pressure decreased to 10 bar, a 12 H-NEC yield of 92.7 % can still be obtained in 32.5 h. To our knowledge, this is the lowest pressure among the results from the reported literatures (Table S1). Meanwhile, the loading of catalyst was also optimized, i.e., the yields of 12 H-NEC were 99.2 % and
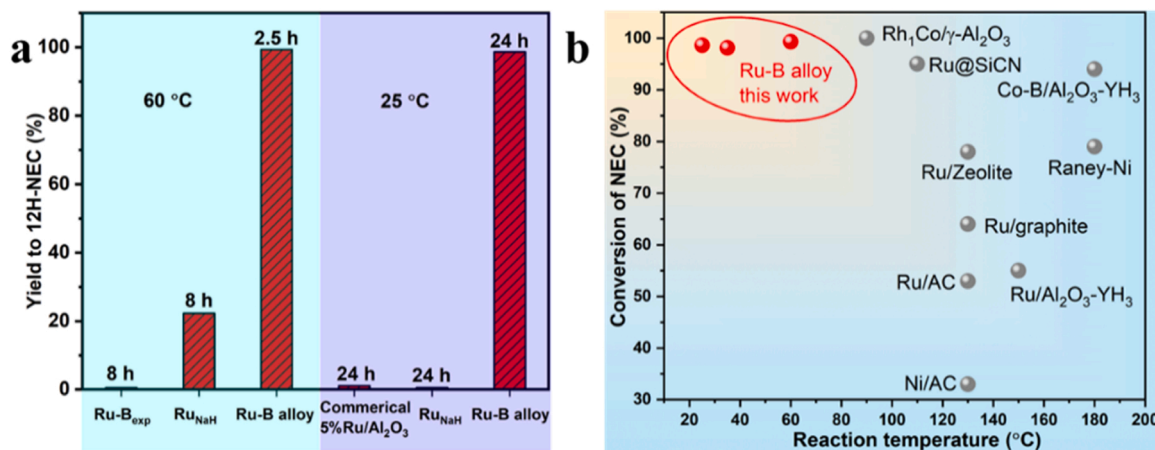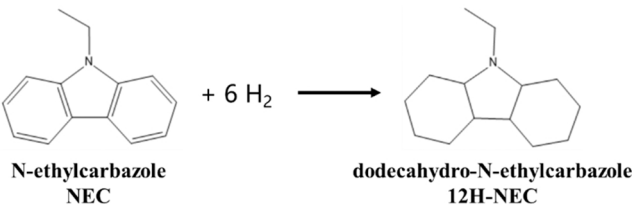

Fig. 3. (a) Comparison of the activity of Ru-B$_{exp}$, Ru$_{NaH}$, commercial 5% Ru/Al$_2$O$_3$, and Ru-B alloy for the catalytic hydrogenation of NEC at 60 and 25 °C under 70 bar of H$_2$ pressure after 8 or 24 h (2.5 h for Ru-B alloy at 60 °C). The molar ratio of Ru catalyst to NEC was fixed as 1:5. (b) Conversions of NEC using various catalysts and reaction temperatures in selected publications [9,11,19,30,42].

Table 2
Ru-B alloy catalyzed the hydrogenation of N-ethylcarbazole.

N-ethylcarbazole
NEC

dodecahydro-N-ethylcarbazole
12H-NEC

Entry	C:S	T (°C)	P (bar)	Solvent	t (h)	Yield (%)
1	1:5	60	70	-	2.5	99.3
2	1:5	35	70	-	6	98.1
3	1:5	25	70	-	24	98.6
4	1:5	60	50	-	3	93.7
5	1:5	60	30	-	8	99.6
6	1:5	60	10	-	32.5	92.7
7	1:10	60	70	-	8	99.2
8	1:20	60	70	-	8	50.9
9	1:5	60	50	i-C$_3$H$_7$OH	5	99.5
10	1:5	60	50	i-C$_3$H$_7$OH	5	99.2
11	1:5	60	50	i-C$_3$H$_7$OH	5	99.4
12	1:5	40	50	i-C$_3$H$_7$OH	1	27.8
13	1:5	60	50	i-C$_3$H$_7$OH	1	54.3
14	1:5	80	50	i-C$_3$H$_7$OH	1	81.6
15	1:5	100	50	i-C$_3$H$_7$OH	1	90.3

Note: C:S means the molar ratio of Ru catalyst to NEC. Yield refers to the content of 12H-NEC in the products. P, hydrogen pressure; T, reaction temperature; t, reaction time.

50.9 % in 8 h when the molar ratios of Ru-B alloy to substrate were fixed at 1:10 and 1:20, respectively (entries 7 and 8). To reduce the constrain of mass transfer, catalytic hydrogenation was conducted in isopropanol as the solvent. It is shown that the 12 H-NEC yield was 99.5 % in 5 h (entry 9), and the catalyst exhibited a good stability as the yields to 12 H-NEC were all higher than 99 % in every cycle (entries 9–11). The hydrogenation in solvent was also evaluated at various reaction temperatures, and as the temperature increased, the yield of 12 H-NEC increased (entries 12–15). The apparent activation energy was calculated from the Arrhenius plot of the hydrogenation reaction, and it was ca. 32.4 kJ/mol as shown in Fig. S10.

As summarized in Fig. 3b and Table S1, the hydrogenation temperatures of higher than 90 °C were needed in literatures, regardless of noble metals, alloys, or composite catalysts were employed. In contrast, the Ru-B alloy catalyst developed here exhibits superior activity at temperature range of 25–60 °C and low hydrogen pressure when compared with Ru nanoparticles, commercial Ru/Al$_2$O$_3$, and reported catalysts, benefiting its energy efficiency for practical application. The higher activity and the lower activation energy could be attributed to the low-coordination sites and tunable electronic structures of Ru metal on the surface of Ru-B alloy. NEC and H$_2$ could be activated appropriately on these low-coordinated and electron-rich Ru sites. Moreover, XRD, TEM, and SAED were employed to characterize the catalyst after the hydrogenation reaction (Fig. 1i and S5 – S7). It is found that the used catalyst still possessed amorphous short-range order structure, and the particles did not appear to have aggregated.

3.3. Mechanism of catalytic hydrogenation of NEC on Ru-B alloy

It is accepted that the superb performance of metastable amorphous alloy in catalysis can be assigned to its exposure of low-coordination sites due to the long-range disorder nature, and tunable electronic structures of metal because of their diverse composition and structure. In the present study, XRD, XAS, and TEM results have clearly confirmed the nanosized amorphous state of Ru-B alloy, which may provide a high concentration of low-coordination sites for catalytic hydrogenation. Furthermore, the explosive nature of Ru-B indicates the metastable state and highly active surface of Ru-B alloy. Electron-rich state of Ru in Ru-B alloy was identified by XPS, in which it was resulted from the electron transfer from B to the underfilled orbital of Ru 3d [37]. Therefore, we calculated the charges transfer between Ru and B using Natural Bond Orbital (NBO) analysis in a Ru-B cluster. As shown in Fig. S7, B is obviously positively charged, while Ru adjacent to B is negatively charged, showing the electron transfer from B to Ru, which derived from the difference in their electronegativities and agrees well with the XPS results. As such, the electron-rich Ru may facilitate the electron transfer from 3d orbital to the antibonding orbital of the aromatic ring in NEC, aiding in the breaking of C=C double bond.

In this work, we explored the lattice plane of Ru$_7$B$_3$ crystal [32], which closely resembles the composition of the Ru-B alloy for possible catalytic active site and further understanding of Ru-B alloy catalytic mechanism through density function theory (DFT) calculations. First, we identified two catalytic active sites on lattice planes (0001) and (10$\bar{1}$0), respectively, based on low-coordination Ru atom position and NEC substrate adsorption energy. As shown in Fig. 4a and c, cluster models of the two active sites were extracted from the crystal structure, and used in the following DFT computation. It is worthy of mention that owing to the nanosized nature of Ru-B alloy particles, a cluster model would be preferable than a slab model. The Gibbs free energy (calibrated to 60 °C and 70 bar) profiles shown in Fig. 4 were obtained at ωB97xD/6–311 +G* *(lanl2dz for Ru)//6–31 G* (lanl2dz for Ru) level of theory [33,34]. The nature of stationary points was verified using frequency analysis. The calculated NEC, H$_2$ co-adsorption on the two active sites were highly exothermic, indicated by adsorption energies of − 59.4 kcal/mol (0001) and − 71.3 kcal/mol (10$\bar{1}$0), respectively. The high adsorption energies here may be attributed to the metastable nature of the selected Ru-B cluster model. We would like to suggest that H$_2$ can be easily dissociated at such active sites. It is shown that the NEC adsorbs on Ru atoms, but it does not directly interact with the B atoms in the clusters. Moreover, the adsorption of NEC depends significantly on the metal-π, in which upon absorption, some of the aromatic C−C bond lengthened from the original 1.39 Å to 1.42–1.45 Å, while the aromatic C−N bonds increased in length from 1.38 Å to 1.40 Å, indicating the activation of these bonds (Fig. S9).

The adsorption state undergoes a two-step hydrogen atom transfer process in order to obtain the partially hydrogenated intermediate,
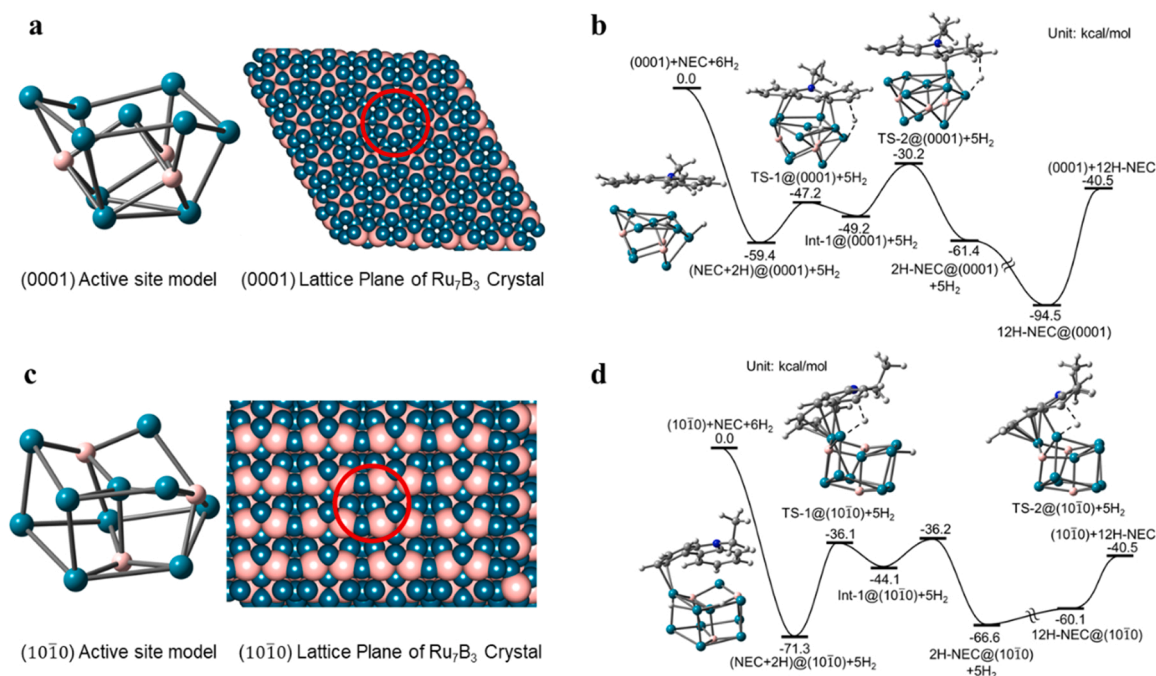
Fig. 4. Active site model and DFT calculated free energy profile of NEC hydrogenation reaction path. (a) $Ru_{10}B_3$ cluster model extracted from Ru_7B_3 crystal (0001) lattice plane; (b) Free energy profile obtained using (0001) active site model; (c) $Ru_{10}B_3$ cluster model extracted from Ru_7B_3 crystal (10$\bar{1}$0) lattice plane; (d) Free energy profile obtained using (10$\bar{1}$0) active site model. Ru, jasper; B, pink; C, gray; N, blue; H, white.

dihydro-N-ethylcarbazole (2H-NEC). The barrier height of the initial hydrogenation step for the (0001) site (12.1 kcal/mol) was significantly lower than that of (10$\bar{1}$0) site (35.2 kcal/mol). Furthermore, the second hydrogenation step recorded a barrier height of 29.2 kcal/mol, which was also lower than that of the (10$\bar{1}$0) site (35.1 kcal/mol). For both active site models, the two C atoms at sites of 3 and 4 were first to be hydrogenated, rather than the carbon atoms (C1 and C6) in the heterocycle (Fig. S9). To further validate the theoretical calculations, we collected the hydrogenation products experimentally at different stages (Fig. S11), and we found that the hydrogenation indeed occurred at the benzene ring, which is consistent with both our simulations and the results from literatures [15,17]. We suggest that the first and second hydrogen atoms transfer should be the rate-determining step. The remaining hydrogenation steps were relatively easier owing to the breaking of aromaticity of NEC. Therefore, they were omitted from Fig. 4 for simplicity. The full hydrogenation of NEC to 12H-NEC on (0001) site model was estimated to be 35.1 kcal/mol exothermically, whereas the full hydrogenation of NEC to 12H-NEC on (10$\bar{1}$0) site model was predicted to be 11.2 kcal/mol endothermically. Based on the above results, we deduce that the (0001) site is more active than the (10$\bar{1}$0) site, and that the calculated barrier height of the NEC hydrogenation catalyzed at the (0001) site well coincides with experimental data. Thenceforth, the (0001) site is probably widespread on the surface of ultrafine Ru-B alloy, and is crucial for NEC hydrogenation.

4. Conclusion

In summary, a one-pot method to prepare ultrafine amorphous metastable Ru-B alloy was developed, which simplifies the synthetic procedures of traditional Ru-B alloys as described in literatures. Interestingly, the as-prepared Ru-B alloy is in a metastable state and would even explode after being dried, which may be attributed to the rapid oxidation of nano B to B_2O_3 and transformation of Ru from amorphous particles to single crystals. More importantly, room temperature hydrogenation of NEC, which has never been accomplished under such low temperatures in the past, was successfully achieved in the presence of

the metastable Ru-B alloy. Meanwhile, the hydrogenation pressure at 60 °C can be reached as low as 10 bar. The high exposure of low-coordination sites and unique electronic structure of the metastable Ru-B alloy may be responsible for its high catalytic activity. Theoretical simulations showed that the hydrogenation of NEC may take place at the (0001) surface of Ru_7B_3 alloy, and the first step of hydrogenation initiated from the benzene ring in NEC, which is consistent with our experimental results. The accomplishment of hydrogenation of NEC under such mild conditions (i.e., room temperature and low pressure) could inevitably decrease the energy consumption during hydrogen storage, and also shed light on the design of novel and efficient catalysts for hydrogenation and other reactions.

CRediT authorship contribution statement

Qijun Pei: Investigation, Methodology, Funding acquisition, Writing – original draft. **Jiafeng Yu**: Formal analysis, Writing - Review & Editing. Guanghao Qiu: Investigation, Methodology. **Khai Chen Tan**: Formal analysis, Methodology. **Junfeng Wen**: Formal analysis, Methodology. **Yang Yu**: Formal analysis, Methodology. **Jintao Wang**: Formal analysis, Methodology. **Jiaquan Guo**: Formal analysis, Methodology. **Jianping Guo**: Formal analysis, Methodology. **Li Rao**: Investigation, Writing - Review & Editing. **Teng He**: Supervision, Funding acquisition, Writing - Review & Editing. **Ping Chen**: Formal analysis, Methodology, Supervision.

Declaration of Competing Interest

The authors declare that they have no known competing financial interests or personal relationships that could have appeared to influence the work reported in this paper.

Data availability

Data will be made available on request.

Acknowledgments

Appendix A. Supporting information

Supplementary data associated with this article can be found in the online version at doi:10.1016/j.apcatb.2023.122947.

References

[1] M. Niermann, S. Drünert, M. Kaltschmitt, K. Bonhoff, Liquid organic hydrogen carriers (LOHCs) – techno-economic analysis of LOHCs in a defined process chain, Energy Environ. Sci. 12 (2019) 290–307.

[2] C. Dong, Z. Gao, Y. Li, M. Peng, M. Wang, Y. Xu, C. Li, M. Xu, Y. Deng, X. Qin, F. Huang, X. Wei, Y.-G. Wang, H. Liu, W. Zhou, D. Ma, Fully exposed palladium cluster catalysts enable hydrogen production from nitrogen heterocycles, Nat. Catal. 5 (2022) 485–493.

[3] P. Preuster, C. Papp, P. Wasserscheid, Liquid organic hydrogen carriers (LOHCs): toward a hydrogen-free hydrogen economy, Acc. Chem. Res. 50 (2017) 74–85.

[4] Q.-L. Zhu, Q. Xu, Liquid organic and inorganic chemical hydrides for high-capacity hydrogen storage, Energy Environ. Sci. 8 (2015) 478–512.

[5] T. He, Q. Pei, P. Chen, Liquid organic hydrogen carriers, J. Energy Chem. 24 (2015) 587–594.

[6] G.P. Pez, A.R. Scott, A.C. Cooper, H. Cheng, Hydrogen storage by reversible hydrogenation of pi-conjugated substrates, United States, 2008.

[7] F. Sotoodeh, K.J. Smith, Kinetics of hydrogen uptake and release from heteroaromatic compounds for hydrogen storage, Ind. Eng. Chem. Res. 49 (2010) 1018–1026.

[8] Z. Wang, I. Tonks, J. Belli, C.M. Jensen, Dehydrogenation of N-ethyl perhydrocarbazole catalyzed by PCP pincer iridium complexes: evaluation of a homogeneous hydrogen storage system, J. Organomet. Chem. 694 (2009) 2854–2857.

[9] K.M. Eblagon, D. Rentsch, O. Friedrichs, A. Remhof, A. Zuettel, A.J. Ramirez-Cuesta, S.C. Tsang, Hydrogenation of 9-ethylcarbazole as a prototype of a liquid hydrogen carrier, Int. J. Hydrog. Energy 35 (2010) 11609–11621.

[10] F. Sotoodeh, L. Zhao, K.J. Smith, Kinetics of H_2 recovery from dodecahydro-N-ethylcarbazole over a supported Pd catalyst, Appl. Catal. A-Gen. 362 (2009) 155–162.

[11] Y. Wu, Y. Guo, H. Yu, X. Jiang, Y. Zhang, Y. Qi, K. Fu, L. Xie, G. Li, J. Zheng, X. Li, Nonstoichiometric yttrium hydride–promoted reversible hydrogen storage in a liquid organic hydrogen carrier, CCS Chem. 2 (2020) 974–984.

[12] Y. Wu, H. Yu, Y. Guo, Y. Zhang, X. Jiang, B. Sun, K. Fu, J. Chen, Y. Qi, J. Zheng, X. Li, Promoting hydrogen absorption of liquid organic hydrogen carriers by solid metal hydrides, J. Mater. Chem. A 7 (2019) 16677–16684.

[13] Y. Wu, H. Yu, Y. Guo, X. Jiang, Y. Qi, B. Sun, H. Li, J. Zheng, X. Li, A rare earth hydride supported ruthenium catalyst for the hydrogenation of N-heterocycles: boosting the activity via a new hydrogen transfer path and controlling the stereoselectivity, Chem. Sci. 10 (2019) 10459–10465.

[14] X. Yang, Y. Wu, H. Yu, M. Sun, J. Zheng, X. Li, W. Lin, Y. Wu, A YH_3 promoted palladium catalyst for reversible hydrogen storage of N-ethylcarbazole, Int. J. Hydrog. Energy 45 (2020) 33657–33662.

[15] T. Zhu, M. Yang, X. Chen, Y. Dong, Z. Zhang, H. Cheng, A highly active bifunctional Ru–Pd catalyst for hydrogenation and dehydrogenation of liquid organic hydrogen carriers, J. Catal. 378 (2019) 382–391.

[16] H. Yu, X. Yang, Y. Wu, Y. Guo, S. Li, W. Lin, X. Li, J. Zheng, Bimetallic Ru-Ni/TiO₂ catalysts for hydrogenation of N-ethylcarbazole: role of TiO₂ crystal structure, J. Energy Chem. 40 (2020) 188–195.

[17] W. Xue, H. Liu, B. Mao, H. Liu, M. Qiu, C. Yang, X. Chen, Y. Sun, Reversible hydrogenation and dehydrogenation of N-ethylcarbazole over bimetallic Pd-Rh catalyst for hydrogen storage, Chem. Eng. J. 421 (2021), 127781.

[18] B. Wang, P.-y Li, Q. Dong, L.-q Chen, H.-q Wang, P.-l Han, T. Fang, Bimetallic NiCo/AC catalysts with a strong coupling effect for high-efficiency hydrogenation of N-ethylcarbazole, ACS Appl. Energy Mater. 6 (2023) 1741–1752.

[19] W. Xue, H. Liu, B. Zhao, L. Ge, S. Yang, M. Qiu, J. Li, W. Han, X. Chen, Single Rh₁Co catalyst enabling reversible hydrogenation and dehydrogenation of N-ethylcarbazole for hydrogen storage, Appl. Catal. B-Environ. 327 (2023), 122453.

[20] L. Ge, M. Qiu, Y. Zhu, S. Yang, W. Li, W. Li, Z. Jiang, X. Chen, Synergistic catalysis of Ru single-atoms and zeolite boosts high-efficiency hydrogen storage, Appl. Catal. B-Environ. 319 (2022), 121958.

[21] K.C. Tan, T. He, Y.S. Chua, P. Chen, Recent advances of catalysis in the hydrogenation and dehydrogenation of N-heterocycles for hydrogen storage, J. Phys. Chem. C 125 (2021) 18553–18566.

[22] A. Baiker, Metallic glasses in heterogeneous catalysis, Faraday Discuss. Chem. Soc. 87 (1989) 239–251.

[23] W.E. Brower, M.S. Matyjaszczyk, T.L. Pettit, G.V. Smith, Metallic glasses as novel catalysts, Nature 301 (1983) 497–499.

[24] W. Cai, R. Chen, H. Yang, H.B. Tao, H.-Y. Wang, J. Gao, W. Liu, S. Liu, S.-F. Hung, B. Liu, Amorphous versus crystalline in water oxidation catalysis: a case study of NiFe alloy, Nano Lett. 20 (2020) 4278–4285.

[25] H. Bi, X. Tan, R. Dou, Y. Pei, M. Qiao, B. Sun, B. Zong, Ru–B nanoparticles on metal–organic frameworks as excellent catalysts for hydrogenation of benzene to cyclohexane under mild reaction conditions, Green Chem. 18 (2016) 2216–2221.

[26] J. Liu, S. He, C. Li, F. Wang, M. Wei, D.G. Evans, X. Duan, Confined synthesis of ultrafine Ru-B amorphous alloy and its catalytic behavior toward selective hydrogenation of benzene, J. Mater. Chem. A 2 (2014) 7570–7577.

[27] Y. Pei, G. Zhou, N. Luan, B. Zong, M. Qiao, F. Tao, Synthesis and catalysis of chemically reduced metal–metalloid amorphous alloys, Chem. Soc. Rev. 41 (2012) 8140–8162.

[28] Z. Zhang, B. Zandkarimi, A.N. Alexandrova, Ensembles of metastable states govern heterogeneous catalysis on dynamic interfaces, Acc. Chem. Res. 53 (2020) 447–458.

[29] G. Sun, P. Sautet, Metastable structures in cluster catalysis from first-principles: structural ensemble in reaction conditions and metastability triggered reactivity, J. Am. Chem. Soc. 140 (2018) 2812–2820.

[30] D. Forberg, T. Schwob, M. Zaheer, M. Friedrich, N. Miyajima, R. Kempe, Single-catalyst high-weight% hydrogen storage in an N-heterocycle synthesized from lignin hydrogenolysis products and ammonia, Nat. Commun. 7 (2016) 13201.

[31] D. Grozea, A. Turak, X.D. Feng, Z.H. Lu, D. Johnson, R. Wood, Chemical structure of Al/LiF/Alq interfaces in organic light-emitting diodes, Appl. Phys. Lett. 81 (2002) 3173–3175.

[32] B. Aronsson, E. Stenberg, J. ÅSelius, Borides of ruthenium, osmium and iridium, Nature 195 (1962) 377–378.

[33] J.-D. Chai, M. Head-Gordon, Long-range corrected hybrid density functionals with damped atom–atom dispersion corrections, Phys. Chem. Chem. Phys. 10 (2008) 6615–6620.

[34] M.J. Frisch, G.W. Trucks, H.B. Schlegel, G.E. Scuseria, M.A. Robb, J.R. Cheeseman, G. Scalmani, V. Barone, B. Mennucci, G.A. Petersson, H. Nakatsuji, M. Caricato, X. Li, H.P. Hratchian, A.F. Izmaylov, J. Bloino, G. Zheng, J.L. Sonnenberg, M. Hada, M. Ehara, K. Toyota, R. Fukuda, J. Hasegawa, M. Ishida, T. Nakajima, Y. Honda, O. Kitao, H. Nakai, T. Vreven, J.A. Jr. Montgomery, J.E. Peralta, F. Ogliaro, M. Bearpark, J.J. Heyd, E. Brothers, K.N. Kudin, V.N. Staroverov, T. Keith, R. Kobayashi, J. Normand, K. Raghavachari, A. Rendell, J.C. Burant, S.S. Iyengar, J. Tomasi, M. Cossi, N. Rega, J.M. Millam, M. Klene, J.E. Knox, J.B. Cross, V. Bakken, C. Adamo, J. Jaramillo, R. Gomperts, R.E. Stratmann, O. Yazyev, A.J. Austin, R. Cammi, C. Pomelli, J.W. Ochterski, R.L. Martin, K. Morokuma, V.G. Zakrzewski, G. A. Voth, P. Salvador, J.J. Dannenberg, S. Dapprich, A.D. Daniels, O. Farkas, J.B. Foresman, J.V. Ortiz, J. Cioslowski, D.J. Fox, Gaussian 09, revision d.01, Gaussian, Inc., Wallingford CT, 2013.

[35] B.-J. Liaw, S.-J. Chiang, C.-H. Tsai, Y.-Z. Chen, Preparation and catalysis of polymer-stabilized NiB catalysts on hydrogenation of carbonyl and olefinic groups, Appl. Catal. A-Gen. 284 (2005) 239–246.

[36] J. van Wonterghem, S. Mørup, C.J.W. Koch, S.W. Charles, S. Wells, Formation of ultra-fine amorphous alloy particles by reduction in aqueous solution, Nature 322 (1986) 622–623.

[37] H.B. Guo, H.X. Li, J. Zhu, W.H. Ye, M.H. Qiao, W.L. Dai, Liquid phase glucose hydrogenation to D-glucitol over an ultrafine Ru-B amorphous alloy catalyst, J. Mol. Catal. A-Chem. 200 (2003) 213–221.

[38] W. Cai, H. Yang, J. Zhang, H.-C. Chen, H.B. Tao, J. Gao, S. Liu, W. Liu, X. Li, B. Liu, Amorphous multimetal alloy oxygen evolving catalysts, ACS Mater. Lett. 2 (2020) 624–632.

[39] Y. Guo, S. Mei, K. Yuan, D.-J. Wang, H.-C. Liu, C.-H. Yan, Y.-W. Zhang, Low-temperature CO₂ methanation over CeO₂-supported Ru single atoms, nanoclusters, and nanoparticles competitively tuned by strong metal–support interactions and H-spillover effect, ACS Catal. 8 (2018) 6203–6215.

[40] M.S. El-Eskandarany, A. Inoue, Mechanically induced cyclic metastable phase transformations of Zr₂Ni alloys, Phys. Lett. B 75 (2007), 224109.

[41] Y. Pal, V.R. Kumar, Thermal decomposition study of paraffin based hybrid rocket fuel containing aluminum and boron additives, Thermochim. Acta 655 (2017) 63–75.

[42] X. Ye, Y. An, G. Xu, Kinetics of 9-ethylcarbazole hydrogenation over Raney-Ni catalyst for hydrogen storage, J. Alloy. Compd. 509 (2011) 152–156.